

Title: Chemically distinct, stable and long-lived thermochemical reservoirs in Earth's deep mantle

Authors: Chunpeng Zhao¹, Edward J. Garnero^{1,*}, Allen K. McNamara¹, Nicholas Schmerr², and Richard W. Carlson³

Affiliations:

¹School of Earth and Space Exploration, Arizona State University, Tempe, Arizona 85287-6004, USA.

²NASA Goddard Space Flight Center, Planetary Geodynamics Laboratory, Greenbelt, MD 20771, USA.

³Department of Terrestrial Magnetism, Carnegie Institution of Washington, 5241 Broad Branch Road, NW, Washington, DC 20015-1305, USA

*Correspondence to: garnero@asu.edu

Abstract: Nearly antipodal continent-sized zones of reduced seismic shear wave velocities exist at the base of Earth's mantle, one beneath the Pacific Ocean, the other beneath the South Atlantic Ocean and Africa. Geophysicists have attributed the low velocity zones to elevated temperatures associated with large-scale mantle convection processes, specifically, hot mantle upwelling in response to cooler subduction-related downwelling currents. Hypotheses have included superplumes, isochemical heterogeneity, and stable as well as metastable basal thermochemical piles. Thus their true nature has remained elusive. Here we seismically image the structure of the low velocity province beneath the Pacific and identify sharp sides as well as a sloping sharp top to the feature. This sharp boundary morphology is consistent with geodynamic predictions for a stable thermochemical reservoir. The peak of the imaged pile is directly below Hawaii, further supporting the presence of a whole mantle plume beneath the hotspot. Lowermost mantle reservoirs can sequester as well as contribute trace element

signatures to plumes and the mantle, and hence are important in the evolution of our planet.

One Sentence Summary: The shape of the deep mantle low shear velocity province beneath the Pacific suggests a thermochemically distinct origin that is dynamically stable, and plays a fundamental role in whole mantle circulation, including mantle plumes.

Main Text:

The present-day chemistry and dynamics of Earth's deep mantle relate to how the mantle as a whole operates, today as well as in the past, including processes relating to the formation and evolution of the planet's core. The behavior of the deep mantle also may influence a number of surface phenomena ranging from driving large-volume intraplate volcanism to regulating the frequency of magnetic reversals. Data that help to constrain our understanding of the deep interior span the geo-disciplines, but seismology provides the most direct means of imaging deep structural features across a range of spatial scales.

Large low shear velocity provinces

Seismic tomography has revealed the presence of two nearly antipodal large low shear velocity provinces (LLSVPs) at the base of the mantle (1-4). These LLSVPs are located beneath Africa and the Pacific, regions that exhibit numerous surface hotspots and are far removed from deep extensions of current and geologically recent subduction

(Fig. 1A). An apparent anti- or non-correlation between bulk and shear modulus in some LLSVP regions (1) along with suggestion of increased density (5,6) support the possibility that they may be compositionally-distinct from the background lower mantle.

The strongest horizontal gradients in tomographically derived shear velocity occur at the LLSVP margins, which coincide with sharp transitions (50-100 km or less) found in high-resolution seismic studies (7-13) (Fig. 1B, Fig. S1). These high-resolution analyses primarily rely upon pulse-broadening of seismic waves that traverse the lowest ~100-200 km of the mantle (Fig. S2, see also Table S1). This pulse-broadening occurs when seismic energy travels both outside and inside the LLSVP, and often results in two distinct arrivals.

The vertical extent of LLSVP structure up off the core-mantle boundary (CMB), including sharp edges, has also been inferred by seismic wave travel times in several studies (13-15). However, these studies assume a shear velocity reduction within the LLSVP, thus a trade-off is present in imaged LLSVP height (and shape). Thus, while the geographical distribution of reduced shear velocities in the lowest couple hundred km appear fairly well established (15), LLSVP structure up into the lower mantle is less so.

Dynamical considerations

If the LLSVPs are regions that are compositionally distinct from the surrounding, background lower mantle, this indicates that the mantle is undergoing thermochemical convection in which dynamics are controlled by both thermal expansion and intrinsic density variations (8,16,17). Geodynamical calculations have demonstrated the

feasibility that Earth's subduction history would act to sweep and focus intrinsically more-dense lower mantle material into the LLSVP regions (18,19) (Fig. 1C). Furthermore, the observation that the surface locations of hotspots (20) and reconstructed origination locations of large igneous provinces (21) preferentially occur over LLSVP margins is consistent with predictions from numerical convection experiments that include thermochemical piles. Some geodynamical studies indicate that plumes may arise from the edges of thermochemical piles (22,23), or alternatively, near the margins of an accumulation of smaller thermochemical piles (18,24).

The morphology of deep mantle structures depends critically upon the differences between density and viscosity properties of the LLSVP material versus the surrounding mantle (18,22,25). Several possible dynamical frameworks are presented in Fig. 2. Each of the four possibilities in Fig. 2 holds promise in matching the two principle seismic observations of significant shear velocity reductions in the LLSVP and sharp LLSVP sides. However, detailed seismic imaging is needed to distinguish between very different predicted geometries for the slope of the LLSVP sides and the top. For example, in a purely isochemical mantle, large-scale convection patterns are expected to focus mantle plumes (perhaps into plume clusters) within larger-scale upwelling regions (Fig. 2A) (18,26-29). However, subducted oceanic lithosphere (30,31), ultra-low velocity zone (ULVZ) material (32), and reaction products between the mantle and core (33) are expected to introduce small-scale heterogeneity into the upwelling, plume regions (Fig. 2B).

The LLSVPs have long been hypothesized to be caused by large-scale, compositionally-distinct structures (8,17,34-37). A critical question relates to the

stability of these structures. If the LLSVPs have a low enough density contrast with the surrounding background mantle, the resulting structures will become unstable and form oscillating thermochemical superplumes that undergo episodes of rising within the mantle, cooling, and then descending back into the lower mantle (34) (Fig. 2C). For higher density contrasts, the resulting structures are expected to remain stable and long-lived (35,36). The morphology of long-lived stable structures is expected to be ridge-like with sloped sides that terminate at a cusp where plumes form (Fig. 2D). Tan and Gurnis (*ref.* 37) demonstrate the formation of “metastable” structures with vertical sides caused by the LLSVPs having a different bulk modulus from the surrounding mantle (Fig. 2C). Stable or metastable piles would possess a seismically detectable top. Isochemical plume clusters, however, should have low seismic wave speeds that extend upwards, lacking an abrupt top to the velocity reductions. The scenarios depicted in Fig. 2 also differ from each other in several other phenomena, including: heat flow from the core, capacity to sequester and provide the compositionally distinct source materials of ocean island basalts (OIBs) compared to mid-ocean ridge basalts (MORBs), and the nature and distribution of small scale heterogeneity. The purpose of this work is to image in high resolution the northwestern portion of the Pacific LLSVP that directly underlies the Hawaiian hotspot (Fig. 1).

High-resolution seismic imaging

We analyze seismic data that densely samples the Pacific LLSVP beneath Hawaii, and combine our results with seismic models of structure from the surface to the deep mantle. Past studies of LLSVP edges (Table S1, Fig. 1) focused on the lowermost 100-

200 km of the mantle. Here we seek to illuminate mantle structure further up off the CMB to investigate the LLSVP margin there. This requires S-wave data that penetrate into the lower mantle with turning depths in the lowest 1000 km of the mantle (within and above the tomographically imaged LLSVP). For the shallower parts of this depth range, epicentral distances between 75 and 85 degrees become necessary. Earthquakes in the southwest Pacific and seismic stations on the west coast of North America make possible interrogation of the Pacific LLSVP beneath Hawaii using this distance range; EarthScope's USArray data (<http://earthscope.org>) figure prominently in this study. The USArray stations permit sampling the deep mantle beneath Hawaii with unprecedented wave path density. Stations in the central and eastern United States have wave paths that sample bottom in the lowest 100-200 km of the mantle, thus, while we include those, we focus more on the western US stations (Fig. S3). We collected 8500 seismograms from 11 intermediate- to deep-focus (>120 km) Fiji-Tonga earthquakes (Table S2).

Waveform broadening was quantitatively determined for our dataset. We developed an iterative stacking algorithm to define an empirical source wavelet shape for each earthquake (see Methods), effectively a mean wave shape for each earthquake that simultaneously documents wave shape and travel time anomalies for individual records of each event. This objectively identifies broadened waveform pulse-widths relative to the empirical source wavelet, and a “misfit” estimate that characterizes the difference between the wave shape of each S-wave and that of the empirical wavelet. Relatively narrow or broadened records have negative or positive misfit values, respectively (see Methods). After discarding records with poor signal quality, our final dataset retained more than 4700 high quality seismograms that densely sample a 30×40 degree area in

the lowermost 1000 km of the mantle beneath the northeastern Pacific (Fig. S3).

Fig. 3 presents an example of normal versus broadened waveforms for an earthquake in our dataset, and demonstrates the concept of our misfit measurement. A more complete set of waveforms, misfits, and travel times for this event are shown in Fig. S4. Waveform misfits and travel time delays for our entire dataset are summarized in Fig. 4. Several features are apparent: (1) significant scatter is present, consistent with the levels of heterogeneity previously identified beneath the central Pacific (38); (2) waveform misfits on average are greatest some 600 km above the CMB (Fig. 4C); and (3) travel time delays are greatest in the lowest 400 km of the mantle. These data enable investigation of LLSVP structure beneath Hawaii further up from the CMB than previously possible.

If LLSVPs have a distinct top due to compositional heterogeneity, there will be an accompanied seismic waveform effect. For example, consider an 800 km thick LLSVP (Fig. 5A). A seismic wave at 80 degrees epicentral distance will have an additional arrival that reflects from the underside of the LLSVP top (Fig. 5B); this additional wave arrives after the direct S wave and broadens the S pulse, and is apparent in the misfit measurements (Fig. 5C and 5D). Thus the top of an LLSVP, if possessing contrasting seismic properties, is detectable with underside reflected S-waves. The misfit and travel time predictions in Fig. 5D are not dissimilar from the averaged measurements of our data set sampling below Hawaii (Fig. 4C): the misfit distribution has a peak at a depth below which the travel time delays begin increasing.

The azimuthal span of our data (Fig. S3) permits us to investigate variations in the Pacific LLSVP in the NW-to-SE direction (Fig. 1A, Fig. S5). Spatial patterns in

waveform misfits are clearly present (Fig. 6A), which, to the first order, outline the upper edge of the LLSVP imaged in tomography (Fig. 6A). Large misfits along the well-sampled NW and SE edges trend diagonally up the LLSVP and connect at a depth of about 600 km above the CMB, which appears to correspond to the top of the tomographically derived LLSVP. This pattern also compares well with the temperature field from a 3-D numerical convection model (Fig. 6C) with a dense basal compositionally-distinct reservoir (24), where an initially uniform dense basal layer is assumed (255 km thick; thicker or thinner layers result in larger or smaller piles, respectively), with 119 Ma of plate motions imposed at the surface. Misfit patterns cannot be due to the earthquake source or receiver regions because events are distributed up and down the Fiji-Tonga trench, whereas misfits have geometric consistencies with their spatial distribution of waveform broadening near their bottoming depths. However, S-waves bottoming in the lowest 200 km of the mantle are close in time to the core-reflected ScS (Fig. 5C), which can result in erroneously large misfits for distances beyond 95 degrees. Furthermore, the presence of a strong velocity change at the LLSVP top produces an additional arrival that propagates just above the LLSVP, at first as a refraction and then as a diffraction, which further contaminates the misfit measurement of waves bottoming in the lowest 200 km of the mantle (Fig. S6).

For a narrow azimuthal portion of the cross-section (shaded region, Fig. 6A), the depth distribution of the misfit averages (Fig. 6D) and time delay averages (Fig. 6E) are simultaneously modeled by a least squares fit to predictions from our 1D model database (Fig. S7). Misfit and travel time anomalies measured from synthetics depend strongly on basic LLSVP properties. Misfit amplitude depends strongly upon the strength of LLSVP

velocity reduction. The sharpness of the top of the LLSVP affects the epicentral distance range (and hence wave bottoming depth) in which the misfit is maximum. LLSVP overall thickness also relates to the distance corresponding to maximum misfit. In general, travel time anomalies are largest for deeper diving waves owing to longer path lengths inside the LLSVP. The best-fitting model (see green lines in Fig. 6D and 6E) is a 600 km thick LLSVP with a constant 1.5% shear velocity reduction, and the LLSVP top distributed over 100 km (Fig. 6F). The broadened waveforms are visible in single records, but also in stacked data for the shaded region of Fig. 6A (Fig. S8). While we expect the shear velocity structure inside the LLSVP to be variable (due to variable temperature and possibly composition), the 1D model approximates the general trend of the data reasonably well.

The travel times are under-predicted for the deeper diving waves; this is not unexpected: we explored constant velocity reduction LLSVPs in the 1-D modeling with emphasis on the waveform effects of the LLSVP top. Towards the CMB the shear velocities have been shown to reduce significantly in this region (39,40). Assuming constant seismic properties within the LLSVP can bias predictions of seismic ray path, and hence bias the imaged shape of LLSVPs, particularly for studies that rely on travel times to map the shape. Here, we map the shape with pulse-broadening information, and do not expect strong dependency upon reference model (Fig. S9).

The large misfits near 600 km above the CMB in the cross-section of Fig. 6A are therefore consistent with the top of the LLSVP in the 1-D model; strong misfits above this depth may correspond to a morphological ridge of the compositional reservoir – a feature seen in the geodynamic modeling and argued for in the African LLSVP (41).

Although less strong and sharp than that used in modeling of the African LLSVP (e.g. -3 % over 50 km (8)), our imaged reduction is nearly twice that inferred from double-array stacking our study region (42). Some waveform misfits outside of the highlighted azimuthal sector are larger, consistent with a greater sharpness to the LLSVP top, and/or a great drop in LLSVP velocities there (i.e., a greater velocity contrast at the LLSVP edge).

LLSVPs and mantle plumes

Mantle plumes are hypothesized to sample material distinct from the upper mantle sources of MORBs. Some plumes bring recycled crustal components back to the surface while others supply material with chemical properties (particularly low $^4\text{He}/^3\text{He}$ ratios) expected for primitive mantle distinct from that of the incompatible element depleted mantle source of MORB, that is, the chemical complement to the incompatible element enriched continental crust (43,44). The creation of new compositional heterogeneity and the preservation of ancient heterogeneity in the mantle depends upon the efficiency of the mixing accompanying mantle convection to homogenize chemically distinct material introduced into the mantle by plate subduction, or remaining from the initial differentiation of the Earth.

With the largest buoyancy flux of any intraplate hotspot on Earth (45), the Hawaiian archipelago serves as an important test bed for various hypotheses regarding plume and source reservoir morphology, as well as mantle circulation and mixing. Seismic tomography supports Hawaii being the surface expression of a long-lived, deep-

rooted mantle plume (46,47), but incomplete data coverage results in blurring of actual structures (48), especially in the lowermost mantle. Waveform analyses have also long speculated that the core-mantle boundary (CMB) may be the source region of the Hawaiian plume (20,21,49). One possibility is that plumes are associated with the margins of LLSVPs, rather than the LLSVP's themselves (20,21). The structure and dynamics of the mantle play an important role in governing plume morphology, from the plume root to the surface, but remain poorly constrained. Hawaii is situated above our LLSVP study region. The distribution of misfits shows a topographic peak of the LLSVP beneath Hawaii. Past tomographic models have low velocities that extend downwards beneath Hawaii to our triangular shaped LLSVP at the base of the mantle (46,47), which is also apparent in larger scale global models (2-4) (Fig. 7A).

The Hawaiian plume hypothesis is further supported by the upper mantle phase discontinuities at 410 and 660 km depth being perturbed in a manner consistent with elevated temperature (50) (Fig. 7B): the 410 discontinuity is deeper and the 660 discontinuity is shallower. We project the waveform misfit measurement of each record to the lowermost 50 km of the seismic ray path (e.g., the paths as in Fig. S3), and then volumetrically average them on a 3-D grid framework (Fig. 7C). We are unable to resolve structure above the 1980 km depth slice due to reduced data coverage (this would require sensors at smaller epicentral distances, but we are limited by the western edge of the North American continent – there are not sensors to the west of this). There is smoothing in the SW-to-NE direction due to lack of crossing ray paths. However, distinct trends are apparent: large waveform misfits are found near the tomographically inferred LLSVP margin, and as the LLSVP forms a peak up off of the CMB, the large misfits

follow this trend and slope upwards towards a peak located beneath the surface position of the Hawaiian hotspot (Fig. 7C). The peak also geographically coincides with the bottom of the tomographically imaged low-shear velocity conduit, consistent with a whole mantle plume originating from the topographic peak of the Pacific LLSVP.

The relative stability of the Hawaiian hot spot (in the last ~80-100 My) may be due to stability in its feeding source – a plume rooted at the top of the Pacific LLSVP. The shape of the northeast portion of the Pacific LLSVP inferred from our waveform misfits is triangular in cross-section, comparable to the shape of long-lived dense compositionally-distinct thermochemical piles in numerical (18,35,36) and laboratory (51) experiments, in which thermal plume upwellings are rooted at cusps along pile ridges (e.g., Fig. 6C). If the intrinsic density of reservoir material is high enough for the piles to be long-lived at the CMB, material entrainment can occur at such ridge cusps (51,52), and such entrained material may explain the trace element and isotopic distinctions between Hawaiian lavas and MORB (43,53). If the entire reservoir is positively buoyant, the whole pile can rise up into the mantle as a superplume (Fig. 2C), which can similarly have sharp sides in the lowermost 1000 km of the mantle. Two important challenges remain for the superplume possibility: the morphology of the top of a superplume is predicted to be dome-shaped (34), not a triangular ridged-top pile as seen here and in other geodynamic studies (18,35,36,51). Secondly, if significant quantities of the LLSVP material are entrained into general mantle circulation, the imaged LLSVPs are either small remnants of originally much larger compositionally distinct reservoirs, or there must be a means to restock the LLSVP's if their volumes have not changed much over Earth history. Thus the longevity of superplumes are likely limited, and it is unclear

how many oscillations a superplume may undergo before being fully stirred into the background mantle.

Uncertainty in model parameters makes a direct comparison between geodynamical models and the actual Earth fraught with difficulty. However, to first order, the strong chemical and thermal gradients at reservoir margins observed in the models (Fig. 6C) agrees with patterns of broadened waveforms near the LLSVP edges observed here (also, see Fig. 1C). Models having dense material swept into piles (e.g., Fig. 2D) consistently display the hottest temperatures along the CMB immediately inside the piles at their boundary with the surrounding lower mantle (54). This is where flow from both within and outside the pile converges at the boundary, and these regions may be the most likely locations for ULVZs (52,55), small patches of material proposed to contain partial melt (52). While the seismic confirmation of ULVZs preferentially occurring at LLSVP margins is promising, it is not unequivocal, and in fact it is not straight forward to conclude dynamical flow in the deep mantle from the distribution of present-day hotspots, subduction zones, ULVZs, and LLSVPs (see Fig. S10). Lateral variability in viscous stress may produce a slightly heterogeneous distribution of ULVZs along thermochemical pile margins, thus ULVZs may be intermittent along LLSVP margins. Whether or not ULVZs are chemically distinct from background mantle and thermochemical pile material, ULVZs should migrate towards thermochemical pile edges, and hence their distribution may demark both the locations of hottest mantle, as well as contain detailed information about LLSVP margins. Some ULVZs are seen outside LLSVPs (Fig. S10), and hence may indicate either that the source of ULVZ material is not limited to LLSVP locations, e.g., such as byproducts of the mantle

chemically reacting with the core (56), or that there is more than one kind of ULVZ. If ULVZs are more likely to be found beneath hotspots (57), then there may be a coupling between processes responsible for thermochemical pile margin morphology giving rise to plumes, and the hottest temperatures of basal mantle rock.

Our seismic imaging finds a sloped side to the LLSVP similar to Fig. 2D. Triangular shaped piles are predicted by both numerical and experimental geodynamics when the thermochemical pile material is intrinsically denser than the mantle rock (i.e., the pile is dynamically stable). More dome-shaped features can occur if the pile material has a higher intrinsic viscosity than the background mantle (17,34,36).

LLSVP origin and chemistry

The constitution of the LLSVPs is uncertain. Hypotheses include remnant material from early Earth differentiation associated with extensive mantle melting – a magma ocean episode for the mantle accompanying Earth formation (58-61), subducted and accumulated oceanic crust reheated by its own radioactive heat generation (30), and accumulated products from chemical reactions between the mantle and core (56). LLSVPs may be relatively dense (5,6) and compositionally distinct from the background lower mantle, and geologically long-lived. If primordial, LLSVPs may be the source of compositionally primitive material feeding hotspots like Hawaii.

A key question is whether any of the LLSVP material is entrained into the portion of the mantle plume that rises and melts beneath hotspots like Hawaii. Hawaiian lavas have low $^4\text{He}/^3\text{He}$ compared to MORB (62), as do many plume-related ocean island

basalts (63), which indicates a mantle component that has not been as significantly outgassed of its primordial noble gas abundances as has the upper mantle sources of MORB. On the other hand, Hawaii also has lavas whose composition suggests a source containing significant amounts of recycled basaltic oceanic crust (64) implying that the LLSVP contribution to the Hawaiian plume might contain recycled subducted oceanic crust. Hawaiian lavas also show elevated $^{186}\text{Os}/^{188}\text{Os}$ ratios that were interpreted as reflecting a source component derived from Earth's core (65), a conclusion supported by a higher Fe/Mn ratio in Hawaiian lavas (66). If the low $^4\text{He}/^3\text{He}$ mantle is attributed to mantle unaffected by or isolated from the process of the extraction of continental crust, a process responsible for the incompatible element depletion characterizing the MORB source mantle, then the major element composition, and hence density, of the low $^4\text{He}/^3\text{He}$ mantle likely is not sufficiently distinct from MORB source mantle to explain elevated LLSVP density required for dynamic stability.

Adding some portion of core to primitive, low $^4\text{He}/^3\text{He}$, mantle could increase its density and enhance its survival at the base of the mantle in (or as) the LLSVPs, and simultaneously explain the low $^4\text{He}/^3\text{He}$, high $^{186}\text{Os}/^{188}\text{Os}$ and Fe-enriched character of the Hawaiian lavas. Ratios of core-soluble (siderophile) to mantle-soluble (lithophile) elements in mantle-derived volcanic rocks, however, have not changed appreciably over at least the last 3.4 Ga of Earth history (67, 68). This limits the amount of core entrained into the mantle over the last 3.4 Ga to no more than a fraction of a weight percent, which then even more severely restricts the amount of core metal that could be entrained into a single plume like Hawaii. At such small amounts of entrainment, the LLSVP material also could then be the complimentary low $^{142}\text{Nd}/^{144}\text{Nd}$ reservoir suggested by the

superchondritic $^{142}\text{Nd}/^{144}\text{Nd}$ of the accessible mantle (58) because several percent of such material would need to be entrained into mantle circulation to cause a measurable secular change in mantle $^{142}\text{Nd}/^{144}\text{Nd}$ (69). The compositional data for OIB provide few constraints on LLSVP composition if no LLSVP material is entrained in the plumes feeding OIB. If entrained LLSVP is no more than a small fraction of a percent of the plume source, a possible candidate LLSVP material is low $^4\text{He}/^3\text{He}$, low $^{142}\text{Nd}/^{144}\text{Nd}$ material containing a small fraction of core metal. If the LLSVP material is the primary constituent of the Hawaiian plume, then the LLSVP under Hawaii likely is dominated by recycled oceanic lithosphere, again with the possibility of a very minor component of incorporated core material.

A discrepancy between the heterogeneous shear and compressional velocity structure in the deep mantle has long been recognized (1), that is, the P-velocity variations do not mimic LLSVPs (70). This is consistent with a chemically distinct origin to LLSVPs, possibly with regions of post-perovskite (71) having a different shear velocity signature than that seen by P waves (72). Certainly, numerical models show that small-scale circulation within piles leads to internal thermal heterogeneity within them (37,54), thus compositional heterogeneity is possible, which might include the appearance of isotropic zoning seen in some OIB studies (44,73).

Past and present pile temperature depends upon radiogenic materials in the pile, and heat flow from the core. If the LLSVP's are either undifferentiated mantle, or the complementary incompatible element enriched mantle proposed on the basis on the superchondritic $^{142}\text{Nd}/^{144}\text{Nd}$ of the accessible mantle (58), then they would be enriched in K, U, and Th compared to the MORB mantle. If stable today, deep mantle reservoirs may

be very long-lived (since it would be difficult to un-mix an entrained thermochemical pile). Considering slow erosive processes of the mantle on the pile, the reservoir volume may have been larger in the past, and eroded pile material may be mixed into general mantle as small-scale heterogeneities (74). Both the invariant ratio of siderophile-to-lithophile element ratio of the accessible mantle over most of Earth history (67) and the lack of secular variation in accessible mantle $^{142}\text{Nd}/^{144}\text{Nd}$ over the last 2.7 Ga (69) limit the amount of entrainment of LLSVP into general mantle circulation (that is sampled by ridges) to no more than a fraction of a percent of the mantle volume. If the LLSVP's consist of either mantle that has interacted with core, or a mantle reservoir formed early in Earth history, or a combination of the two, then the current size of the LLSVP's must be similar to their size throughout most of Earth history. If the LLSVP's consist of recycled subducted lithosphere, then their size in the past depends on the rate of incorporation of newly subducted lithosphere compared to their rate of entrainment in mantle plumes. However, uncertainties in rheological properties of LLSVP material compared to the mantle give rise to significant uncertainties regarding the temporal evolution of LLSVP volume.

Geodynamical calculations consistently show the presence of a thermal boundary layer along the surface of thermochemical piles that provide the source of mantle plumes. Thus details of the 3D morphology of piles, e.g., the nature of ridges at pile margins, will govern when and where plumes occur, and how strong, the latter which determines the degree to which plumes and entrain pile material. Variations in subduction-related lower mantle convective currents over long time periods can result in pile reshaping, and even possibly reorganization (52,75).

Our findings argue that tomographically derived, nearly antipodal LLSVPs are chemically distinct, and a nearly vertical mantle plume beneath Hawaii originates from a topographical peak of the northeast region of the compositionally distinct Pacific LLSVP. This reservoir extends some 600-900 km up off the CMB into the overlying mantle. The sloped side of the LLSVP provides evidence that it is a long-lived thermochemical pile. Furthermore, plumes can thus entrain long-lived deep mantle reservoir material leading to isotopic and chemical signatures unique to hotspot volcano basalts.

Methods

To document waveform broadening we define a waveform “misfit” measurement in terms of a percentage of a waveform’s deviation from the mean shape of S-waves on an event by event basis, and determine the travel time perturbation relative to a reference model by the following steps:

(1) *Empirical source wavelet construction.* For each event, a time window from 15 sec before and 30 sec after direct S (or Sdiff) on the transverse component of motion is defined, using predictions from the PREM model (76). The maximum amplitude in this time window is normalized to unity. On displacement recordings, these 45 sec long time windows are linearly summed to make an initial stack. Records with S-waves close in time to ScS are omitted. The initial stack is iteratively updated by the following procedure: (a) each record is aligned with the stack using cross-correlation, and polarity-checked and corrected if necessary; (b) its shift time and cross-correlation coefficient (CCC_Z) is stored; (c) using the CCC_Z ’s as weights, records are summed to make a new stack, omitting any record with $CCC_Z < 0.5$, an empirical value. This iterative procedure, sometimes referred to as adaptive stacking (77), is continued until the updated stack wave shape is nearly identical with the previous stack, as defined by the CCC_Z between a previous and updated stack being greater than 0.999. We define this final stack as the empirical source stack (ESS) for this event. As part of this first step, the discarded ($CCC_Z < 0.5$) and retained records were visually inspected to insure the automation procedure was operating properly.

(2) *Definition of empirical source timing onset.* The ESS was used to estimate the timing of individual records (relative to predictions made with the PREM model). We employ

an algorithm to objectively and automatically define the relative onset timing of the ESS pulse. First, a noise level is defined as the maximum amplitude in a 5 sec long time window, starting 14 sec before the S-wave peak in the ESS. S-wave onsets are typically smooth in the ESS's. Therefore, we take the time derivative of the displacement recording ESS, which sharpens the commencement of the S-wave pulse. The onset is then defined as the time value where the amplitude of the ESS pulse (in velocity) exceeds the pre-determined noise level value. While this approach is empirical, it is robust in that it produces ESS onset times for our event population in a uniform fashion.

(3) *Computation of individual waveform misfit and timing.* For each event, all retained S-waves are cross-correlated with the ESS. They are then windowed from the ESS onset time to an end time defined by 2.5 times the peak-minus-onset time. This adds 50% more time window after the S-wave peak than the onset-to-peak time, which we chose based on inspection of the data, which show steeper ramp up to the peak than decay from the peak (in displacement recordings). The aligned and normalized record and ESS are subtracted; the result is integrated, and then divided by the integrated ESS. We thus define a misfit as the relative difference between the area beneath each record's wave shape and that of the ESS stack for the specified time window, in percent:

$$Misfit = \frac{S_{rec}^i - S_{ESS}}{S_{ESS}} \times 100\%$$

S_{rec}^i stands for the area under the curve of the i^{th} record, and S_{ESS} denotes the area under the curve of the ESS stack. Thus, records narrower or broader than the ESS will have negative or positive misfit values, respectively. Records that are broadened due to wave multi-pathing (8-10) may have contributed to erroneously broadening the ESS, i.e., resulting in an ESS that does not simply represent the earthquake's source time function.

We circumvent this outcome by re-computing Step 2 solely with records containing negative misfit values, resulting in a new empirical source stack, denoted ESS'. ESS' represents the narrowest half of the waveshape population. This population is referred to as the “normal” waveforms (e.g., Fig. 3). Waveform misfit for each record is then re-computed, as defined above, except using ESS'. This process also re-computes the timing anomaly of each S-wave onset, relative to the PREM model predictions.

These choices in windowing and stacking parameters were developed by extensive trial and error tests to achieve the most stable mean shape of each event, i.e., ESS', as well as onset times and misfit measurements across different earthquakes with different source time functions. While subjective, this procedure is consistent across events in how it documents relative waveform broadening and travel time anomalies (Fig. 3).

Synthetic Tests. We computed synthetic seismograms for more than 1,000 one-dimensional (1-D) models using the reflectivity method (78). We varied three principle features associated with a lowermost mantle low velocity region: (a) the velocity reduction magnitude, from 0 to -3.5%, in 0.5% intervals; (b) the sharpness of the transition from “normal” (PREM) overlying mantle to the LLSVP, from 0 to 350 km for the thickness of the gradient zone, in 50 km intervals; and (c) LLSVP thickness, in 50 km increments, defined as the distance from the CMB to the base of the gradient zone (or the discontinuity, if the gradient is zero). Waveform misfits and delay times are shown in Fig. S7 for synthetics measured exactly the same way as the data. They show significant effects depending on the structural details of the LLSVP structure. Larger LLSVP shear velocity reductions yield larger waveform misfits and delay times (Fig. S7A). A 20%

increase in the maximum waveform misfit can be caused by only 0.5% added velocity reduction in the LLSVP. The depth of the peak in the waveform misfit plot depends strongly on LLSVP velocity reduction, but is generally close to that of the discontinuity at the top of the LLSVP. The velocity gradient on top of the LLSVP affects the misfit amplitude and depth range over which the waveform misfit variations occur (Fig. S7B). Thicker velocity gradients result in weaker misfit values, and broadened distribution of misfit values near the depth of the LLSVP top. For a fixed LLSVP velocity reduction and gradient width at the LLSVP top, Fig. S7C shows the dependency of the misfits and travel times on the LLSVP thickness. Fig. 5 shows the synthetic waveforms, measured misfit and travel times for one such model. The details of the misfit measurements are shown to also depend on interfering phases (e.g., ScS).

Best-fitting regional 1-D model. In a grid search fashion, we establish a measure of goodness of fit of each 1-D model to the observations as follows. (a) We compute the cross-correlation coefficient between the depth distribution of predicted and observed misfits (CCC_z); for the observations, we use the depth-bin averages for the correlation. This establishes the degree to which the shapes of the depth distributions agree. (b) We account for the amplitude of the misfit versus depth variation by comparing the peak misfit amplitude of synthetics and observations, and combining with the CCC_z for a measure of goodness of fit:

$$Goodness_of_fit = CCC_z \times \left(1 - \frac{A_s - A_d}{A_d}\right)^2$$

where A_s is the peak misfit amplitude in synthetics and A_d is the peak misfit amplitude in the data averages. We note that the location of S-wave bottoming depths are different distances from the cross-section which we project misfits onto, but not significantly, and

that bottoming depths are not very different from the cross-section piercing depths (Fig. S5).

Fig. S11 provides information on travel times, ray sampling density, and standard deviation of travel times and misfits on the main cross-section investigated in this study. Fig. S12 shows the misfits projected to the cross-section on top of lateral gradients estimated from the tomographic model TBXW (3).

References

1. G. Masters, G. Laske, H. Bolton, A. M. Dziewonski, The relative behavior of shear velocity, bulk sound speed, and compressional velocity in the mantle: implications for chemical and thermal structure, in *Earth's Deep Interior* (eds Karato, S., Forte, A. M., Liebermann, R. C., Masters, G. & Stixrude, L.) 63-87 (Vol. 117, American Geophysical Union, Washington, D. C.) (2000).
2. C. Mégnin, B. Romanowicz, The shear velocity structure of the mantle from the inversion of body, surface, and higher modes waveforms. *Geophys. J. Int.* **143**, 709–728, doi:10.1046/j.1365-246X.2000.00298.x (2000).
3. S. P. Grand, Mantle shear-wave tomography and the fate of subducted slabs. *Phil. Trans. R. Soc. Lond.* **360**, 2475-2491, doi:10.1098/rsta.2002.1077 (2002).
4. J. Ritsema, A. Deuss, H. J. van Heijst, J. H. Woodhouse, S40RTS: a degree-40 shear-velocity model for the mantle from new Rayleigh wave dispersion, teleseismic traveltimes and normal-mode splitting function measurements. *Geophys. J. Int.* **184**, 1223-1236, doi:10.1111/j.1365-246X.2010.04884.x (2011).
5. M. Ishii, J. Tromp, Normal-mode and free-Air gravity constraints on lateral variations in velocity and density of Earth's mantle. *Science* **285**, 1231-1236, doi:10.1126/science.285.5431.1231 (1999).
6. J. Trampert, F. Deschamps, J. Resovsky, D. Yuen, Probabilistic tomography maps chemical heterogeneities throughout the lower mantle. *Science* **306**, 853-856, doi:10.1126/science.1101996 (2004).

7. S. Luo, S. Ni, D. V. Helmberger, Evidence for a sharp lateral variation of velocity at the core–mantle boundary from multipathed PKPab. *Earth Planet. Sci. Lett.* **189**, 155-164, doi:10.1016/S0012-821X(01)00364-8 (2001).
8. S. Ni, E. Tan, M. Gurnis, D. V. Helmberger, Sharp Sides to the African Superplume. *Science* **296**, 1850-1852, doi:10.1126/science.1070698 (2002).
9. A. To, B. Romanowicz, Y. Capdeville, N. Takeuchi, 3D effects of sharp boundaries at the borders of the African and Pacific Superplumes: Observation and modeling. *Earth Planet. Sci. Lett.* **233**, 137-153, doi:10.1016/j.epsl.2005.01.037 (2005).
10. S. R. Ford, E. J. Garnero, A. K. McNamara, A strong lateral shear velocity gradient and anisotropy heterogeneity in the lowermost mantle beneath the southern Pacific. *J. Geophys. Res.* **111**, 1-14, doi:10.1029/2004JB003574 (2006).
11. D. Sun, E. Tan, D. V. Helmberger, M. Gurnis, Seismological support for the metastable superplume model, sharp features, and phase changes within the lower mantle. *Proc. Natl. Acad. Sci.* **104**, 9151-9155, doi:10.1073/pnas.0608160104 (2007).
12. Y. He, L. Wen, Structural features and shear-velocity structure of the “Pacific Anomaly”. *J. Geophys. Res.* **114**, B02309, doi:10.1029/2008JB005814 (2009).
13. J. Ritsema, S. Ni, D. V. Helmberger, H. P. Crotwell, Evidence for strong shear velocity reductions and velocity gradients in the lower mantle beneath Africa. *Geophys. Res. Lett.* **25**, 4245–4248, doi: 10.1029/1998GL900127 (1998).
14. L. Wen, Seismic evidence for a rapidly-varying compositional anomaly at the base of the Earth's mantle beneath the Indian Ocean, *Earth Planet. Sci. Lett.* **194**, 83-95, doi:10.1016/S0012-821X(01)00550-7 (2001).

15. V., Lekic, S. Cottaar, A. Dziewonski, B. Romanowicz, Cluster analysis of global lower mantle tomography: A new class of structure and implications for chemical heterogeneity. *Earth and Planet. Sci. Lett.* **357–358**, 68-77, doi:10.1016/j.epsl.2012.09.014 (2012).
16. P. J. Tackley, Mantle convection and plate tectonics: Toward an integrated physical and chemical theory. *Science* **288**, 2002-2007, doi:10.1126/science.288.5473.2002 (2000).
17. P. J. Tackley, Dynamics and evolution of the deep mantle resulting from thermal, chemical, phase and melting effects. *Earth Sci. Rev.* **110**, 1-25, doi:10.1016/j.earscirev.2011.10.001 (2012).
18. A. K. McNamara, S. Zhong, Thermochemical structures beneath Africa and the Pacific Ocean. *Nature* **437**, 1136-1139, doi:10.1038/nature04066 (2005).
19. N. Zhang, S. J. Zhong, Heat fluxes at the Earth's surface and core-mantle boundary since Pangea formation and their implications for the geomagnetic superchrons. *Earth Planet. Sci. Lett.* **306**, 205-216, doi:10.1016/j.epsl.2011.04.001 (2011).
20. M. Thorne, E. J. Garnero, S. P. Grand, Geographic correlation between hot spots and deep mantle lateral shear-wave velocity gradients. *Phys. Earth Planet. Inter.* **146**, 47-63, doi:10.1016/j.pepi.2003.09.026 (2004).
21. T. H. Torsvik, K. Burke, B. Steinberger, S. J. Webb, L. D. Ashwal, Diamonds sampled by plumes from the core-mantle boundary. *Nature* **466**, 352-355, doi:10.1038/nature09216 (2010).
22. E. Tan, W. Leng, S. Zhong, M. Gurnis, On the location and mobility of thermochemical structures with high bulk modulus in the 3-D compressible mantle.

- Geochem. Geophys. Geosyst* **12**, doi:10.1029/2011GC003665 (2011).
23. B. Steinberger, T.H. Torsvik, A geodynamic model of plumes from the margins of Large Low Shear Velocity Provinces. *Geochem. Geophys. Geosyst.* **13**, doi:10.1029/2011gc003808 (2012).
 24. E. J. Garnero, A. K. McNamara, Structure and dynamics of Earth's lower mantle. *Science* **320**, 626-628, doi:10.1126/science.1148028 (2008).
 25. P. J. Tackley, S. Xie, T. Nakagawa, J. W. Hernlund, Numerical and laboratory studies of mantle convection: Philosophy, accomplishments and thermo-chemical structure and evolution, in *Earth's Deep Mantle: Structure, Composition, and Evolution*, Geophysical Monograph Series 160, AGU, 83-99, doi:10.1029/160GM07 (2005).
 26. G. Schubert, G. Masters, P. Olson, P. Tackley, Superplumes or plume clusters? *Phys. Earth Planet. Int.* **146**, 147-162, doi:10.1016/j.pepi.2003.09.025 (2004).
 27. A. L. Bull, A. K. McNamara, J. Ritsema, Synthetic tomography of plume clusters and thermochemical piles. *Earth Planet. Sci. Lett.* **278**, 152-162, doi:10.1016/j.epsl.2008.11.018 (2009).
 28. B. S. A. Schuberth, H. P. Bunge, J. Ritsema, Tomographic filtering of high-resolution mantle circulation models: Can seismic heterogeneity be explained by temperature alone? *Geochem. Geophys. Geosyst.* **10**, doi 10.1029/2009gc002401 (2009).
 29. D. R. Davies, S. Goes, B. S. A. Schuberth, H. P. Bunge, J. Ritsema, Reconciling dynamic and seismic models of Earth's lower mantle: The dominant role of thermal heterogeneity. *Earth Planet. Sci. Lett.* **353**, 253-269,

- doi:10.1016/j.epsl.2012.08.016 (2012).
30. U. R. Christensen, A. W. Hofmann, Segregation of subducted oceanic crust in the convecting mantle. *J. Geophys. Res.* **99**, 19867–19884, doi:10.1029/93JB03403 (1994).
 31. J. P. Brandenburg, P. E. van Keken, Deep storage of oceanic crust in a vigorously convecting mantle. *J. Geophys. Res.* **112**, doi:10.1029/2006jb004813 (2007).
 32. S. Rost, P. Earle, Identifying regions of strong scattering at the core-mantle boundary from analysis of PKKP precursor energy. *Earth Planet. Sci. Lett.* **297**, 616-626, doi:10.1016/j.epsl.2010.07.014 (2010).
 33. M. Manga, R. Jeanloz, Implications of a metal-bearing chemical boundary layer in D'' for mantle dynamics. *Geophys. Res. Lett.* **23**, 3091-3094, doi:10.1029/96GL03021 (1996).
 34. A. Davaille, Simultaneous generation of hotspots and superswells by convection in a heterogeneous planetary mantle. *Nature* **402**, 756-760, doi:10.1038/45461 (1999).
 35. P. J. Tackley, Strong heterogeneity caused by deep mantle layering. *Geochem. Geophys. Geosystems*. **3**, doi:10.1029/2001GC000167 (2002).
 36. A. K. McNamara, S. Zhong, Thermochemical structures within a spherical mantle: Superplumes or Piles? *J. Geophys. Res.* **109**, B07402, doi:10.1029/2003JB002847 (2004).
 37. E. Tan, M. Gurnis, Metastable superplumes and mantle compressibility. *Geophys. Res. Lett.* **32**, L20307, doi:10.1029/2005GL024190 (2005).
 38. Y. He, L. Wen, Geographic boundary of the "Pacific Anomaly" and its geometry and

- transitional structure in the north. *J. Geophys. Res.* **117**, B09308, doi:10.1029/2012JB009436 (2012).
39. J. Ritsema, E. J. Garnero, T. Lay, A strongly negative shear velocity gradient and lateral variability in the lowermost mantle beneath the Pacific. *J. Geophys. Res.* **102**, 20395-20411, doi:10.1029/97JB01507 (1997).
40. L. Bréger, B. Romanowicz, Three-dimensional structure at the base of the mantle beneath the central Pacific. *Science* **282**, 718-720, doi:10.1126/science.282.5389.718 (1998).
41. D. Sun, D. Helmberger, M. Gurnis, A narrow mid-mantle plume below southern Africa. *Geophys. Res. Lett.* **37**, L09302, doi:10.1029/2009GL042339, 5 pp. (2010).
42. T. Lay, J. Hernlund, E. J. Garnero, M. S. Thorne, A post-perovskite lens and D" heat flux beneath the central Pacific. *Science* **314**, 1272-1276, doi:10.1126/science.1133280 (2006).
43. A. W. Hofmann, Mantle geochemistry: the message from oceanic volcanism. *Nature* **385**, 219–229, doi:10.1038/385219a0 (1997).
44. D. Weis, M. O. Garcia, J. M. Rhodes, M. Jellinek, J. S. Scoates, Role of the deep mantle in generating the compositional asymmetry of the Hawaiian mantle plume. *Nature Geosci.* **4**, 831-838, doi:10.1038/NGEO1328 (2011).
45. N. H. Sleep, Hotspots and mantle plumes: some phenomenology. *J. Geophys. Res.* **95**, 6715-6736, doi:10.1029/JB095iB05p06715 (1990).

46. R. Montelli, G. Nolet, F. A. Dahlen, G. Masters, E. R. Engdahl, S. H. Hung, Finite-frequency tomography reveals a variety of plumes in the mantle. *Science* **303**, 338-343, doi: 10.1126/science.1092485 (2004).
47. C. J. Wolfe, S. C. Solomon, G. Laske, J. A. Collins, R. S. Detrick, J. A. Orcutt, D. Bercovici, E. H. Hauri, Mantle shear-wave velocity structure beneath the Hawaiian hot spot. *Science* **326**, 1338-1390, doi:10.1126/science.1180165 (2009).
48. J. Ritsema, A. K. McNamara, A. L. Bull, Tomographic filtering of geodynamic models: implications for model interpretation and large-scale mantle structure. *J. Geophys. Res.* **112**, B01303, doi:10.1029/2006JB004566 (2007).
49. S. Russell, T. Lay, E.J. Garnero, Seismic evidence for small-scale dynamics in the lowermost mantle at the root of the Hawaiian hotspot. *Nature* **369**, 255-257 doi:10.1038/24364 (1998).
50. N. Schmerr, E. J. Garnero, A. K. McNamara, Deep mantle plumes and convective upwelling beneath the Pacific Ocean. *Earth Planet. Sci. Lett.* **294**, 143-151, doi:10.1016/j.epsl.2010.03.014 (2010).
51. A. M. Jellinek, M. Manga, The influence of a chemical boundary layer on the fixity, spacing and lifetime of mantle plumes. *Nature* **418**, 760–763, doi:10.1038/nature00898.1 (2002).
52. A. K. McNamara, E. J. Garnero, S. Rost, Tracking deep mantle reservoirs with ultra-low velocity zones. *Earth Planet. Sci. Lett.* **299**, 1-9, doi:10.1016/j.epsl.2010.07.042 (2010).

53. S. R. Hart, A large-scale isotope anomaly in the Southern Hemisphere mantle. *Nature* **309**, 753–757, doi:10.1038/309753a0 (1984).
54. E. J. Garnero, T. Lay, A. McNamara, Implications of lower mantle structural heterogeneity for existence and nature of whole mantle plumes. In: *The Origin of Melting Anomalies: Plates, Plumes and Planetary Processes*, Foulger, G. R., and D. M. Jurdy (eds.), The Geological Society of America Special Paper 430, p79-101, doi:10.1130/2007.2430(05) (2007).
55. J. W. Hernlund, P. J. Tackley, Some dynamical consequences of partial melting in Earth's deep mantle. *Phys. Earth Planet. Int.* **162**, 149-163, doi:10.1016/j.pepi.2007.04.005 (2007).
56. E. Knittle, R. Jeanloz, Earth's core-mantle boundary: results of experiments at high pressures and temperatures. *Science* **251**, 1438-1443, doi:10.1126/science.251.5000.1438 (1991).
57. Q. Williams, J. Revenaugh, E. Garnero, A correlation between ultra-low basal velocities in the mantle and hot spots. *Science* **281**, 546-549, doi:10.1126/science.281.5376.546 (1998).
58. M. Boyet, R. W. Carlson, ¹⁴²Nd Evidence for early (>4.53 Ga) global differentiation of the silicate Earth. *Science*. **309**, 576-581, doi:10.1126/science.1113634 2005.
59. C. T. Lee, P. Luffi, T. Höink, J. Li, R. Dasgupta, J. Hernlund, Upside-down differentiation and generation of a 'primordial' lower mantle. *Science* **462**, 930-935, doi:10.1038/nature08824 (2010).
60. S. Labrosse, J. W. Hernlund, N. Coltice, A crystallizing dense magma ocean at the base of the Earth's mantle. *Science* **450**, 866-869, doi:10.1038/nature06355

(2007).

61. R. Nomura, H. Ozawa, S. Tateno, K. Hirose, J. Hernlund, S. Muto, H. Ishii, N. Hiraoka, Spin crossover and iron-rich silicate melt in the Earth's deep mantle. *Nature* **473**, 199-202, doi:10.1038/nature09940 (2011).
62. H. Craig, J. E. Lupton, Primordial neon, helium, and hydrogen in oceanic basalts. *Earth Planet. Sci. Lett.* **31**, 369-385, doi:10.1016/0012-821X(76)90118-7 (1976).
63. D. R. Hilton, D. Porcelli, Noble gases as mantle tracers. In *Treatise on Geochemistry* in *Treatise on Geochemistry: The mantle and core*. H. D. Holland, K. K. Turekian, (eds.), Elsevier, Vol. 2: The mantle and core, pp. 277-318 (2003).
64. E. H. Hauri, Major-element variability in the Hawaiian mantle plume. *Nature* **382**, 415-419, doi:10.1038/382415a0 (1996).
65. A. D. Brandon, M. D. Norman, R. J. Walker, J. W. Morgan, ^{186}Os - ^{187}Os systematics of Hawaiian picrites. *Earth Planet. Sci. Lett.* **174**, 25-42, doi:10.1016/S0012-821X(99)00251-4 (1999).
66. M. Humayun, L. Qin, M. D. Norman, Geochemical evidence for excess iron in the mantle beneath Hawaii. *Science* **306**, 91-94, doi:10.1126/science.1101050 (2004).
67. K. P. Jochum, A. W. Hofmann, H. M. Seufert, Tin in mantle-derived rocks - constraints on Earth evolution. *Geochimica et Cosmochimica Acta* **57**, 3585-3595, doi:10.1016/0016-7037(93)90141-I (1993).
68. K. W. W. Sims, H. E. Newsom, E. S. Gladney, Chemical fractionation during formation of the Earth's core and continental crust: clues from As, Sb, W, and Mo. in *Origin of the Earth*, edited by H. E. Newsom, and J. H. Jones, pp. 291-

- 317, Oxford University Press, New York (1990).
69. M. G. Jackson, R. W. Carlson, Homogeneous superchondritic $^{142}\text{Nd}/^{144}\text{Nd}$ in the mid-ocean ridge basalt and ocean island basalt mantle. *Geochem. Geophys. Geosyst.* doi:10.1029/2012GC004114 (2012).
 70. T. Lay, E. J. Garnero, Core-mantle boundary structures and processes. in *The State of the Planet: Frontiers and Challenges in Geophysics*, edited by R. S. J. Sparks and C. J. Hawkesworth, Geophysical Monograph 150, IUGG Volume 19, doi:10.1029/150GM04 (2004).
 71. T. Lay, E. J. Garnero, Reconciling the post-perovskite phase with seismological observations of lowermost mantle structure. in *Post-Perovskite: The Last Mantle Phase Transition*, edited by K. Hirose, J. Brodholt, T. Lay, and D. Yuen, American Geophysical Union, Monograph, 129-153 (2007).
 72. J. Wookey, S. Stackhouse, J. M. Kendall, J. Brodholt, G. D. Price, Efficacy of the post-perovskite phase as an explanation for lowermost-mantle seismic properties. *Nature* **438**, 1004-1007, doi:10.1038/nature04345 (2005).
 73. J. A. Payne, M. G. Jackson, P. S. Hall, Parallel volcano trends and geochemical asymmetry of the Society Islands hotspot track. *Geology* **41**, 19-22, doi:10.1130/G33273.1 (2013).
 74. M. A. H. Hedlin, P. M. Shearer, P. S. Earle, Seismic evidence for small-scale heterogeneity throughout the Earth's mantle. *Nature* **387**, 145-150, doi:10.1038/387145a0 (1997).
 75. M. S. Thorne, E. J. Garnero, G. Jahnke, H. Igel, A. K. McNamara, Mega ultra low velocity zone and mantle flow. *Earth Planet. Sci. Lett.* **364**, 59-67,

- doi:10.1016/j.epsl.2012.12.034 (2013).
76. A. M. Dziewonski, D. L. Anderson, Preliminary reference earth model (PREM). *Phys. Earth Planet. Int.* **25**, 297-356, doi:10.1016/0031-9201(81)90046-7 (1981).
77. N. Rawlinson, B. L. N. Kennett, Rapid estimation of relative and absolute delay times across a network by adaptive stacking. *Geophys. J. Int.* **157**, 332-340, doi:10.1111/j.1365-246X.2004.02188.x (2004).
78. G. Müller, The reflectivity method—A tutorial. *J. Geophys.* **58**, 153– 174 (1985).

Supplementary Online Material

Materials and Methods

Figs. S1-S12

Tables S1-S2

www.sciencemag.org/

Acknowledgements We thank the Incorporated Research Institutions for Seismology (IRIS), the EarthScope USArray, and the Canadian National Seismograph Network for providing us high quality seismograms. This research was supported by NSF.

Author Contributions C.Z. and E.J.G. initiated the project. C.Z. performed the data collection, measurements, and model building with assistances from E.J.G. C.Z. and E.J.G. wrote the paper. A.K.M. supplied the geodynamic model and N.S. provided the transition zone thickness model. R.W.C. developed ideas about the origin of the LLSVPs and contributed knowledge about mantle chemistry. All authors discussed the results and commented on the manuscript.

Author Information Reprints and permissions information is available at www.nature.com/reprints. The authors declare no competing financial interests. Correspondence and requests for materials should be addressed to E.J.G. (garnero@asu.edu).

Figures and Captions:

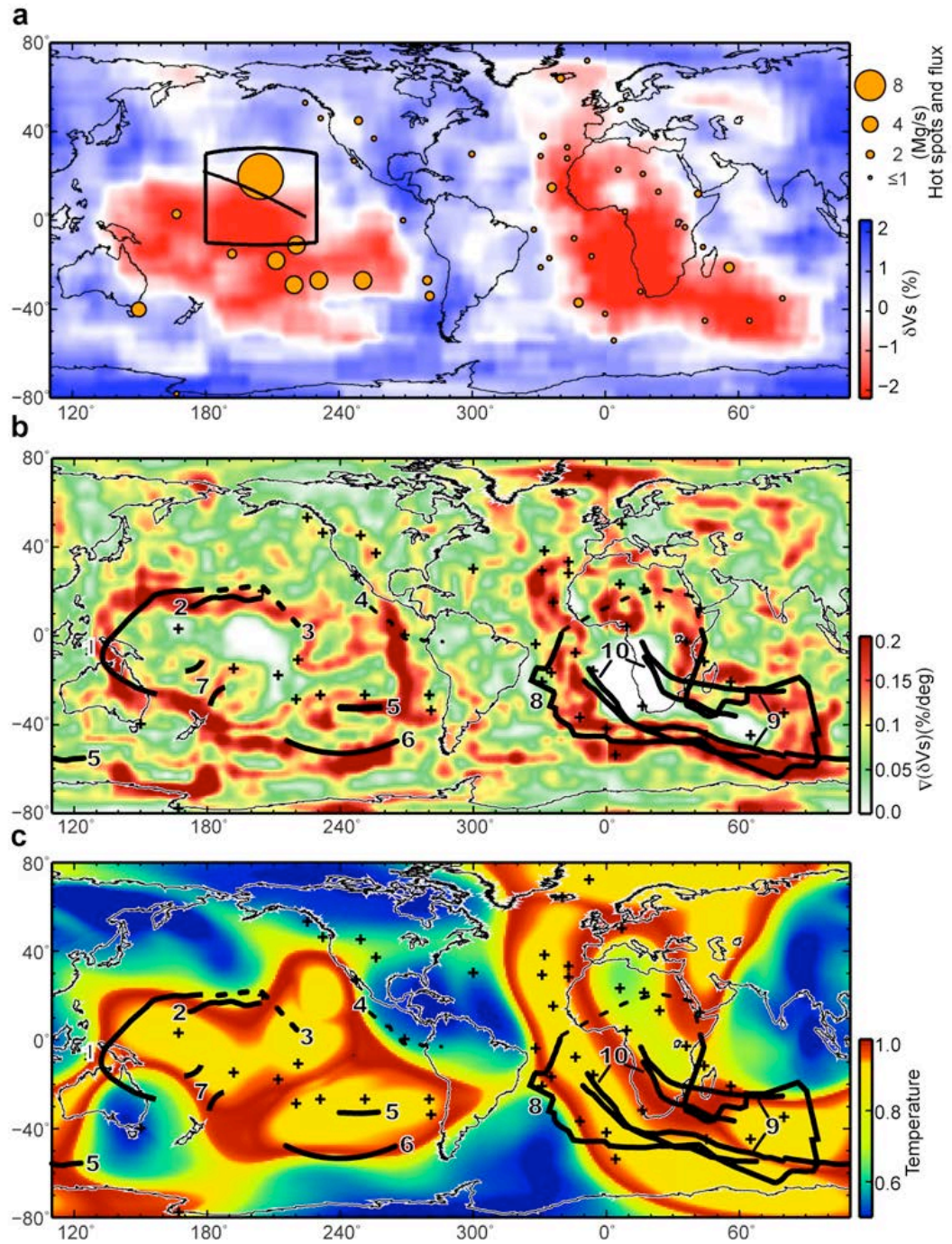


Fig. 1. Geographic correlation between lowermost mantle shear velocity tomography, lateral gradients, and imaged edges. (A) Hotspot locations (orange

circles) are plotted on top of a global tomography shear velocity model TXBW (3) at 2750 km depth. Blue and red colors represent higher and lower velocities, respectively. Hotspot size is scaled to the flux of each hotspot (45). The black box denotes the study region of this paper. The solid black line inside of the box indicates the location of the cross-section in Fig. 6. **(B)** Lateral shear velocity gradients in model TXBW (red = strongest gradients) are plotted with LLSVP edges (thick black lines, dashed if from travel time inference) found in previous studies (numbers in the Fig. correspond to Table S1). Hotspot locations are crosses. Gradients are calculated following a least-square linear curve-fitting algorithm (20). **(C)** Similar to **(B)**, but displayed are lateral variations of the temperature field calculated from a thermochemical convection model (24). Strongest gradients in **(B)** and temperatures in **(C)** are similar – they are near LLSVP margins found in high-resolution studies.

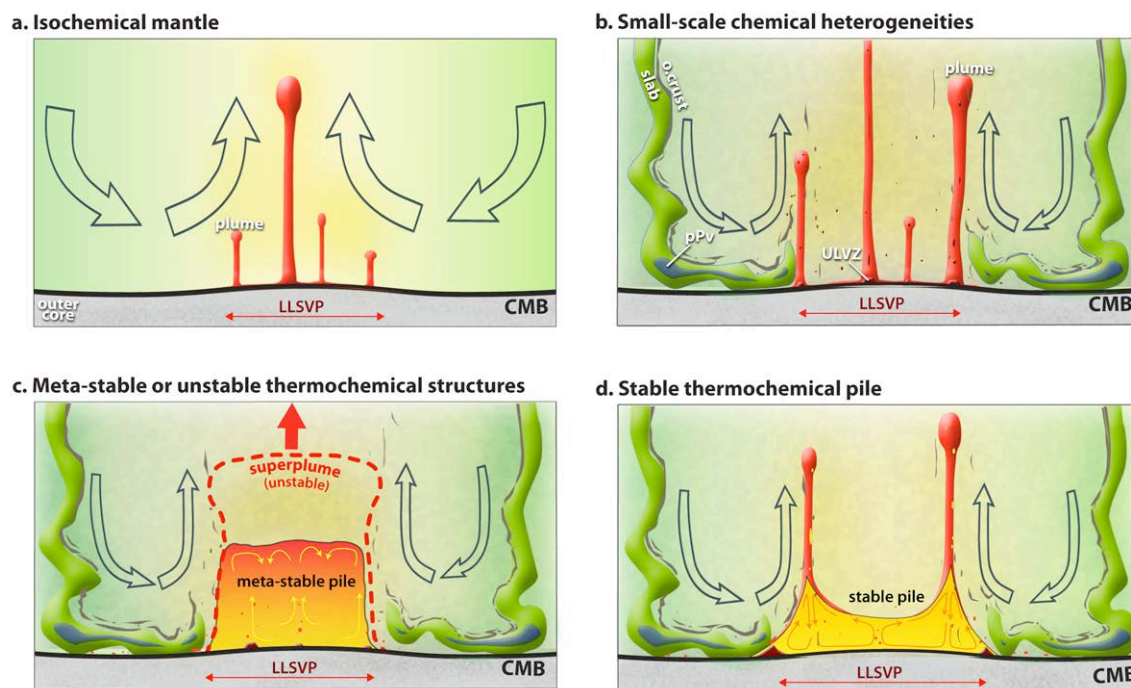


Fig. 2. Scenarios that can result in an LLSVP. (A) In an isochemical mantle, upwelling and plumes can be concentrated in areas away from beneath downwelling, and the warmer upwelling zone can be an LLSVP, though the sides may not be uniformly sharp. (B) Former lithosphere and oceanic crust, as well as ultra-low velocity zone (ULVZ) material can introduce small-scale heterogeneities into the lowermost mantle, and enhance the seismically imaged contrast between the LLSVP and surrounding mantle. (C) A nearly neutrally buoyant thermochemical structure can have vertical sides and a shape that depends strongly on internal properties (called a meta-stable pile). If unstable, the whole structure may break away from the CMB as a superplume (red dashed line). (D) With density slightly elevated, the thermochemical pile becomes a stable structure with sloped sides and plumes coming off ridges. For both (C) and (D), small-scale heterogeneities can mix into the thermochemical material. In all cases, the zone labeled LLSVP will be beneath upwelling, away from cold downwelling zones.

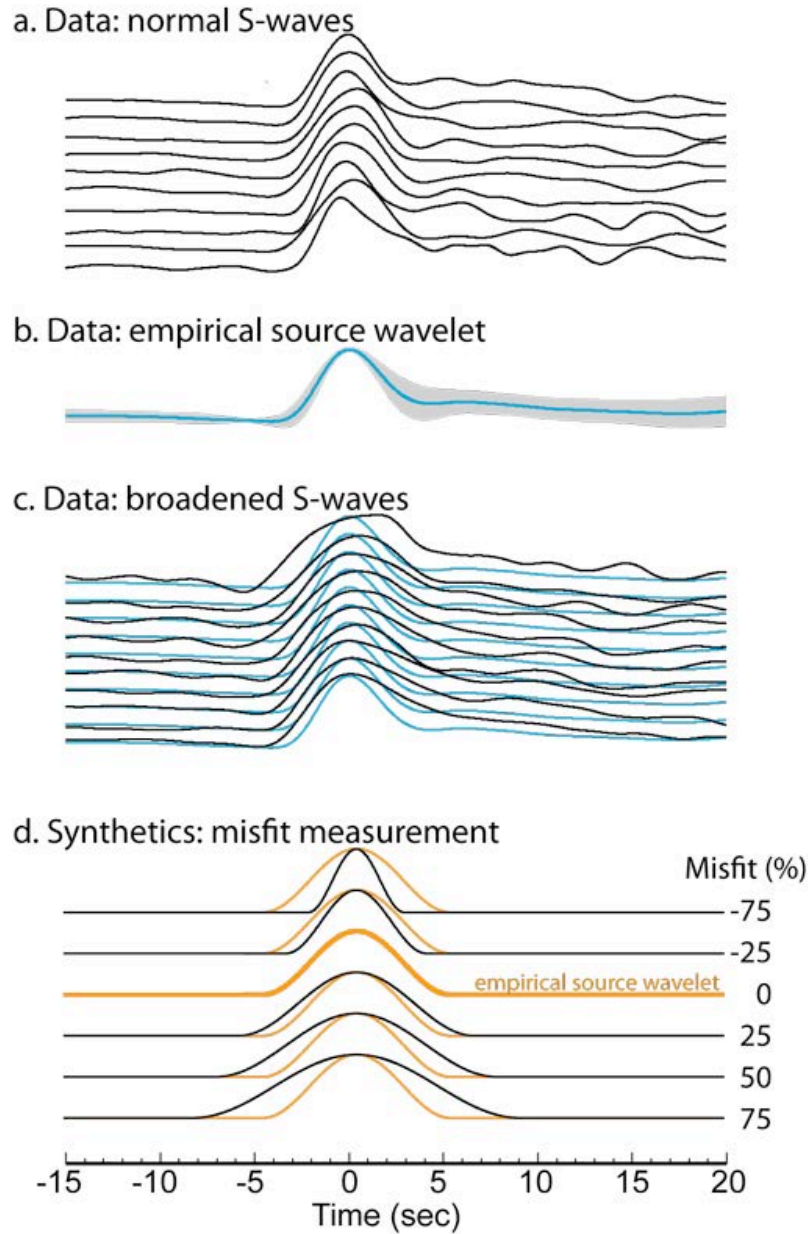


Fig. 3. Waveform examples of misfit measurements. For the earthquake of August 26, 2007, we show (A) ten “normal” waveforms of the S-wave, defined by having a misfit value $\sim 0\%$, and thus closely resemble the empirical source shape shown in (B) (thick black line); gray shading displays the standard deviation of this stack. (C) Similar to (A), except ten broadened waveforms are shown (thin black lines), defined by large misfit values ($\sim 40\%$). Thin gray line traces are the empirical source from (B). (D) This synthetic

example demonstrates the relationship between waveform broadening and misfit value (computed as described in the Method section in the main text) for a simple sinusoid stretched by different amounts. The record with zero % misfit is defined as the empirical source, and is repeated as the gray trace for the non-zero misfit records (which are black). Thus a 100% misfit record is roughly twice as wide as the empirical source shape; a 50% misfit value corresponds to a record roughly $\frac{1}{2}$ as wide as the empirical source shape.

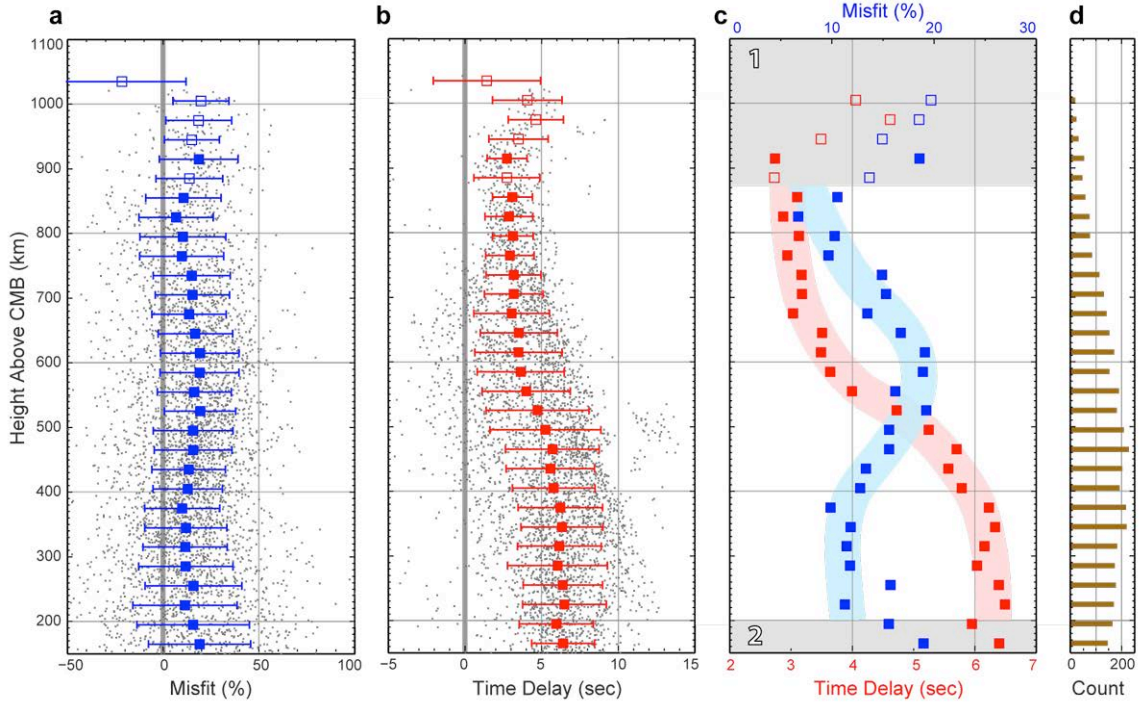


Fig. 4. Waveform misfits and travel time delays for the entire dataset. S-wave waveform misfits and time delays are shown for our entire data set as a function of PREM-predicted wave bottoming depth above the CMB. Individual misfit measurements (A) and travel time delay measurements (B) are gray dots, and are accompanied with mean values in 30 km depth intervals with \pm one standard deviation (horizontal bars). Open squares correspond to 30 km depth intervals with less than 50 data points. Panel (C) compares the mean values from (A) and (B) with slightly expanded horizontal scales. For most of the robustly sampled depth bins, the maximum misfits and travel time delays appear to occur at different depths (near 600 km above the CMB for the misfits, and in the lower 400 km of the mantle for the travel time delays). We omit focus on the two gray regions: region 1 corresponds to too few data, region 2 corresponds to complications in the misfit measurement due to contamination by ScS. (D) Number of records within each 30 km bin.

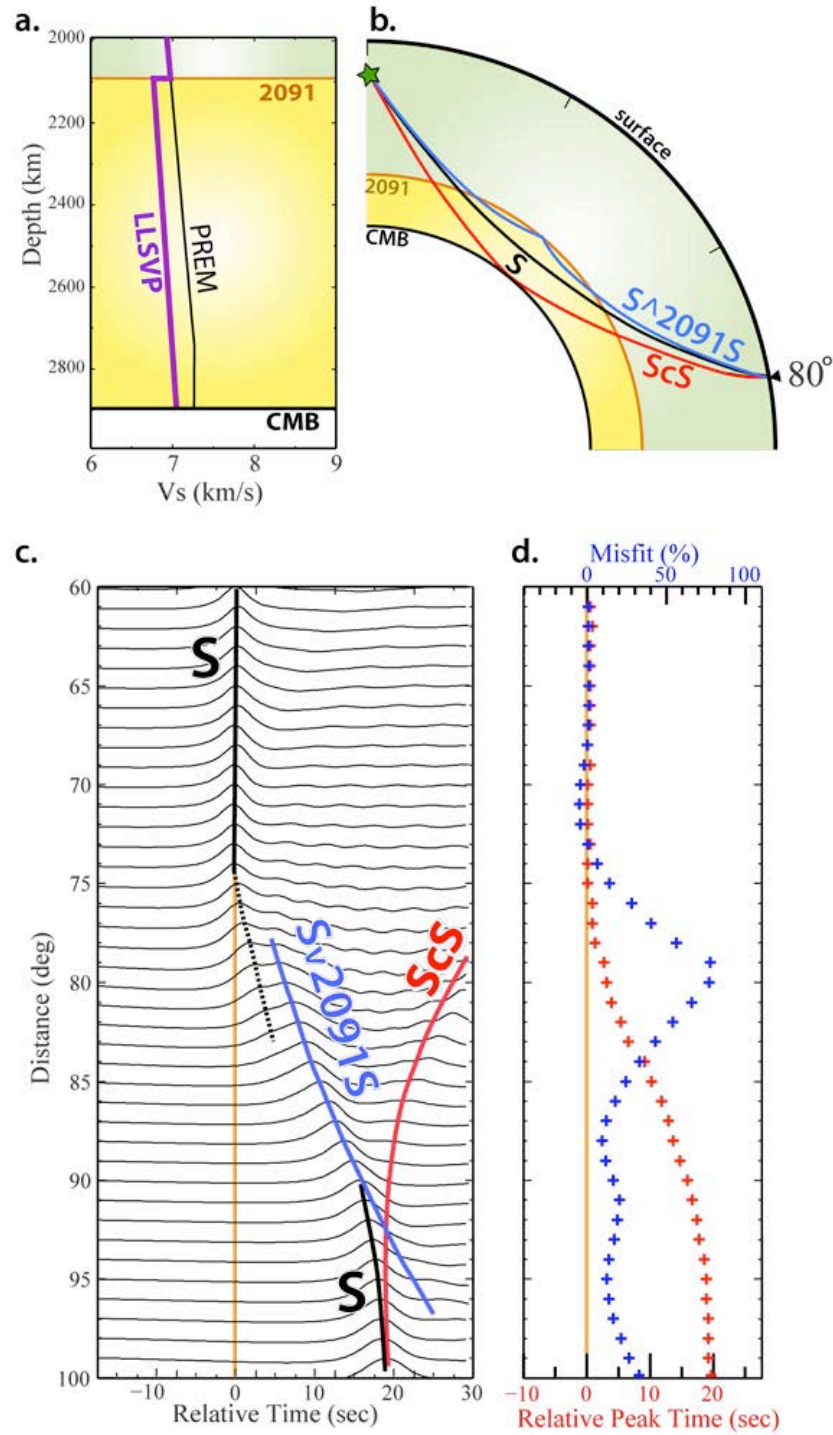


Fig. 5. Synthetics for a lower mantle possessing an LLSVP. (A) Shear velocity-depth profile showing an 800 km thick LLSVP. **(B)** Ray paths of seismic waves that Fig. prominently in the broadening of a deep mantle S-wave: the core reflected ScS and the

wave that reflects from the underside of the top of the LLSVP, here, dubbed S^{2091S} , for an epicentral distance of 80 degrees. **(C)** Reflectivity method (78) displacement synthetic seismograms for the tangential component. Traces are plotted relative to that predicted by the PREM model (76). At around 77 deg the S-wave becomes multi-pulsed due to the S^{2091S} arrival, thus becoming broadened. The wave group is delayed at larger distances due to the reduced shear wave velocities of the LLSVP. **(D)** The misfit (blue) and travel time delays (red) are shown for measurements on the synthetic seismograms of panel **(C)**. As with the observations (Fig. 4), the misfits have a peak several 100 km above the CMB from the LLSVP top, and travel time delays increase for deeper diving waves.

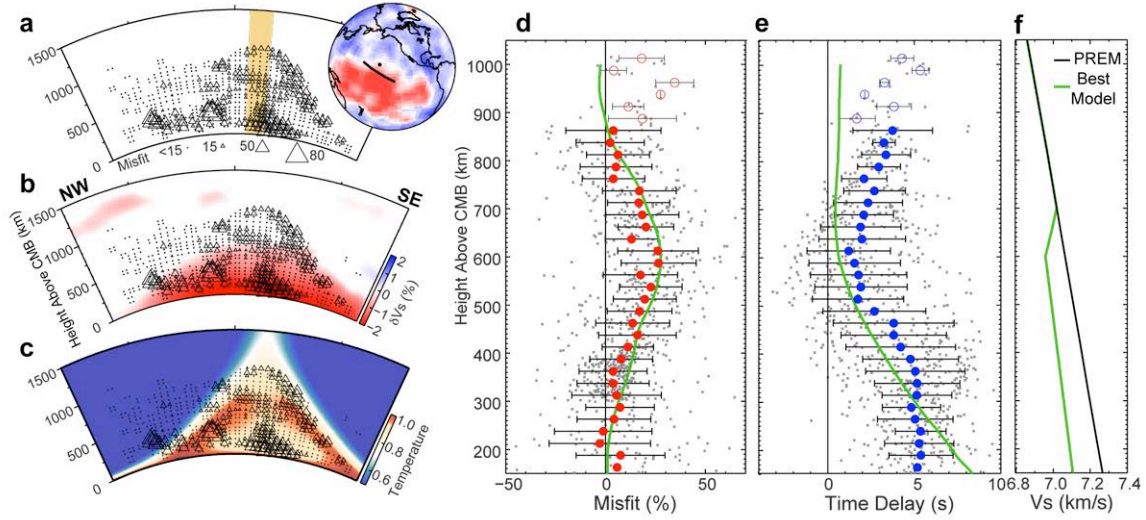


Fig. 6. Waveform misfits cross-section maps and modeling results. (A) A 50-degree wide cross-section (location indicated in Fig. 1A), with misfit values (triangles) projected to cross-section, overlying tomography model TXBW (3). Tan shaded box highlights azimuth range of the data plotted in (D) and (E). (B) As in (A), plotted on top of shear velocity reductions of a mantle tomography model (3). (C) As in (A), plotted on top of a temperature snapshot of a numerical flow model (24), which has a chemically distinct dense pile at the base of the mantle. Misfit values from (A) are plotted on top, and demonstrate the consistency between our observations with the reservoir hypothesis. (D) Misfits (gray dots) and 30 km wide depth-bin averages (red circles, with ± 1 standard deviation) are plotted with respect to the S wave bottoming depth. Open circles represent depth-bins with less than 10 records. Solid red line is a prediction for our best-fitting 1-D reservoir model shown in (F). (E) As in (D) except travel time anomalies are shown (gray dots) with depth-bin averages (blue circles). Solid blue line is the prediction for our best-fitting model shown in (F). (F) Shear velocity versus depth of our best-fitting 1-D reservoir model (red) compared to PREM (black) for data in the shaded azimuth window

in panel (**A**).

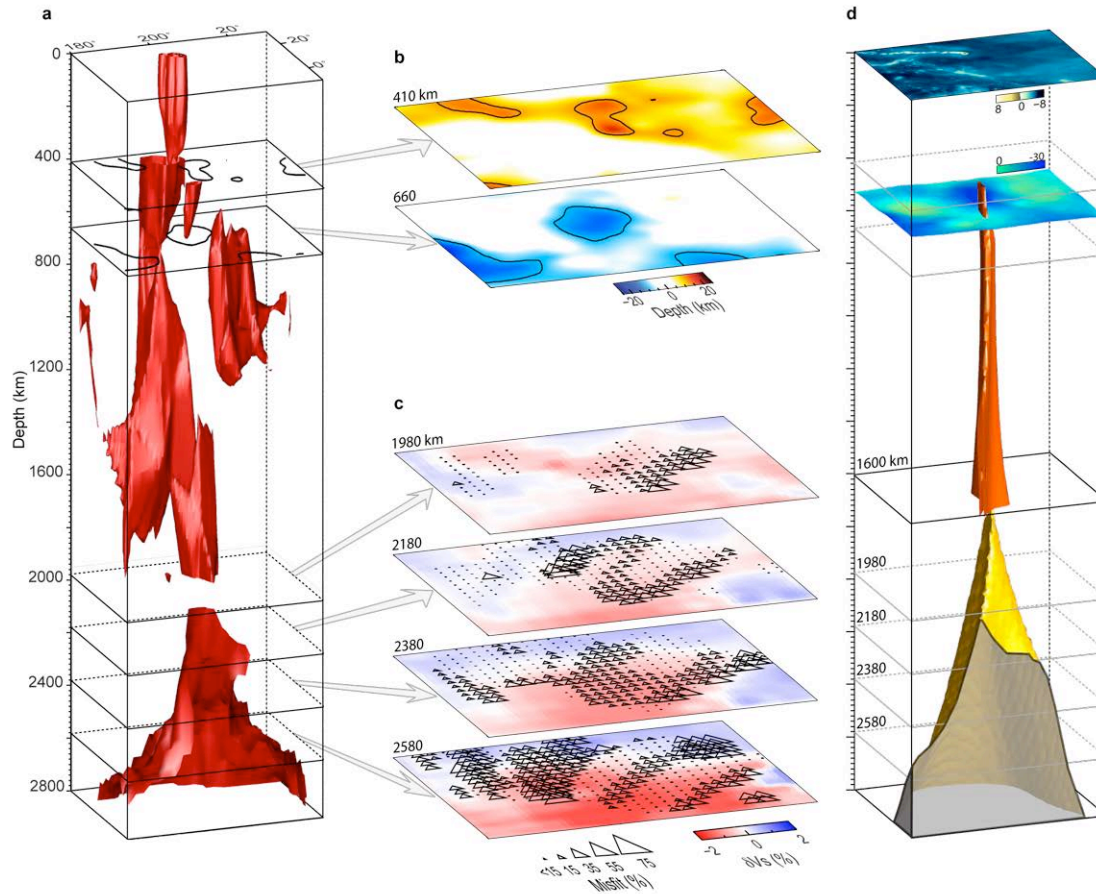


Fig. 7. Correlation of waveform misfits with tomography, transition zone thickness, geodynamic model. (A) 3D iso-surfaces of δV_s tomography for 3 different models. From the surface to about 400 km, the iso-surface is at -1.5% for a regional tomography model (47). From about 400 km to 2000 km, the iso-surface is at -1.0% for another tomography model (46). At 410 and 660 km depth, contours (black lines) for the transition zone discontinuity topography are also plotted (50). Below 2000 km, the iso-surface is at -0.9% for the global tomography model TXBW (3). Black boxes stand for the layer locations shown in the middle panel. **(B)** Discontinuity topography of 410 and 660, along with contours shown in **(A)**. **(C)** Misfit values projected onto every point of the lowermost 50 km segments of PREM-predicted ray paths. Numbers denote the depth of each slice.

We smoothed these path segments over a grid with spacing 2 by 2 deg laterally, and 50 km in the depth direction. The smoothed misfit values (open triangles and black dots) are plotted on top of the shear-wave velocity perturbations of the tomography model TXBW (*Ref. 3*). **(D)** The iso-surface of temperature (orange) for the upper 1600 km of the mantle, and iso-surface of composition (gold) for the rest of the mantle are shown. These iso-surfaces are based upon a geodynamically derived thermochemical convection model with a couple hundred kilometers thick dense layer at the bottom of the mantle (24). The map on the surface is the topography of the Hawaii region. Transition zone thickness estimates (50) are also shown as a surface plotted in between 410 and 660 km depth.